

Radiation Damage of $2 \times 2 \times 1 \text{ cm}^3$ Pixelated CdZnTe Due to High-Energy Protons

Daniel Shy^a, David Goodman^b, Ryan Parsons^b, Michael Streicher^b, Willy Kaye^b, Lee Mitchell^a, Zhong He^b, Bernard Philips^a

^aU.S. Naval Research Laboratory, 4555 Overlook Ave SW, Washington, DC 20375

^bH3D, Inc., 812 Avis Dr, Ann Arbor, MI 48108, USA

Abstract

Pixelated CdZnTe detectors are a promising imaging-spectrometer for gamma-ray astrophysics due to their combination of relatively high energy resolution with room temperature operation negating the need for cryogenic cooling. This reduces the size, weight, and power requirements for telescope-based radiation detectors. Nevertheless, operating CdZnTe in orbit will expose it to the harsh radiation environment of space. This work, therefore, studies the effects of 61 MeV protons on $2 \times 2 \times 1 \text{ cm}^3$ pixelated CdZnTe and quantifies proton-induced radiation damage of fluences up to $2.6 \times 10^8 \text{ p/cm}^2$. In addition, we studied the effects of irradiation on two separate instruments: one was biased and operational during irradiation while the other remained unbiased. Following final irradiation, the 662 keV centroid and nominal 1% resolution of the detectors were degraded to 642.7 keV, 4.9% (FWHM) and 653.8 keV, 1.75% (FWHM) for the biased and unbiased systems respectively. We therefore observe a possible bias dependency on proton-induced radiation damage in CdZnTe. This work also reports on the resulting activation and recovery of the instrument following room temperature and 60°C annealing.

Keywords: CdZnTe, radiation damage, gamma-ray spectroscopy, gamma-ray astrophysics

1. Introduction

Solid state detectors present an advantage over scintillation-based detectors for use in radiation detection applications due to their generally superior energy resolution [1]. This advantage stems from its direct-conversion process as semiconductors generally require less energy to produce an information carrier and result in a smaller fano factor. This results in better energy resolution as they are less limited by statistical fluctuation when compared to their scintillator counterparts. CdZnTe (CZT), a wide band gap, room temperature semiconductor, is a promising high-resolution gamma/x-ray spectrometer for space deployments.

CZT has a significant heritage of being used in space experiments. It has flown in several balloon flights [2, 3, 4] as well as flying in space on instruments such as the BAT-Swift Observatory [5], AstroSat [6], Dawn [7], and ASIM [8]. It is also considered for future missions such as AMEGO [9], GECCO [10], and ASTENA [11].

If the instrument is placed in low earth orbit, it will likely pass through the Southern Atlantic Anomaly (SAA) to some varying degree that depends on orbit inclination [12]. There, it will experience a high flux of trapped energetic particles. The space radiation environment also contains galactic cosmic rays (mostly energetic protons and alphas at 10 GeV/nucleon) and solar-based radiation from solar activity [13]. This radiation environment can severely degrade the performance of gamma-ray spectrometers [14].

In this work, we study the damage induced by 61 MeV protons on CZT. Although the proton flux in the SAA is represented by a power law in between 10 – 100 MeV [15], 61 MeV

protons are still within that range, and therefore somewhat illustrative of the actual environment. Sec. 2 discusses previous work concerning radiation damage in CZT. Sec. 3 is the methods section describing the CZT hardware, the irradiation facility, and the irradiation plan. Sec. 4 presents the results from the proton irradiations and Sec. 5 presents the detector's recovery with annealing. Sec. 6 offers an analysis of the observed activation.

2. Previous Work on High-Energy Proton Irradiation With CZT

Several radiation damage studies on CZT were conducted with protons on the order of several hundred MeV. Varnell et al. irradiated 2 – 3 mm planar CZT with 200 MeV protons [16]. They observed that as the dose increased, the spectral gain decreased proportionally due to the production of electron traps which decreases the mobility lifetime product ($\mu\tau_e$) of electrons. With 3 mm CZT, they observed a shift in the peak centroid with a fluence as low as $1 \times 10^8 \text{ p/cm}^2$ [17]. That same group irradiated pixelated CdZnTe and observed a factor of 4.4 degradation in the $\mu\tau_e$ of the worst detector that experienced $5 \times 10^9 \text{ p/cm}^2$. Franks et al. provide an overview of damage in various room temperature semiconductors [18]. In CZT, they report that planar 3 mm thick CZT exposed to 200 MeV experiences a two-fold loss in energy resolution after a fluence of $5 \times 10^9 \text{ p/cm}^2$ but little effect in 2 mm thick devices. Moreover, when testing 2 mm planar devices they observed larger resolution losses in an unbiased detector when compared to the biased case. The electric field strength, or voltage bias, is not reported in the cited work.

A few years later, Kuvvetli et al. irradiated a 2.7 mm thick drift strip detector with 30 MeV protons [19]. The first irradiation of 2.8×10^8 p/cm² resulted in a noticeable decline in $\mu\tau_e$. They were able to recover the detector after annealing at 100°C for a total time of 22 hours.

Zanarini et al. irradiated 1 mm thick CZT with 2 MeV protons and did not observe any gain shift or resolution change even with an exposure of 10^{11} p/cm² [20].

It is worth noting that the aforementioned detectors were relatively thin, on the order of millimeters. Bolotnikov et al. irradiated larger volume $8 \times 8 \times 32$ mm³ virtual Frisch-grid detectors [21] with 150 MeV protons. Irradiated from the ‘side’, they did not notice any polarization during acquisition with low proton flux of 160 p/cm²/s. During the high flux damage study, they did not notice any gain shift with fluences up to 10^6 p/cm². However, with a fluence of 4×10^7 p/cm², they began noticing a small gain shift of less than 2%. After 10^{10} p/cm², the detectors stopped responding. Nevertheless, the detectors are fully recovered after annealing at 65 °C and then 80 °C for 3 and 2 weeks respectively. During irradiation, their detectors were biased with a field of 115.6 V/mm.

3. Materials and Methods

3.1. CdZnTe Hardware

This work uses two M400 CZT modules [22, 23] manufactured by H3D, Inc. The module utilizes four crystals, each with a volume of $2 \times 2 \times 1$ cm³. The anode contains an array of 11×11 pixels with a pitch of 1.72 mm with a planar cathode. This allows for the 3D reconstruction of interaction positions. The crystals are arranged in a 2×2 array with the cathodes facing towards the incident proton beam.

In this study, the manufacturer calibrated the system beforehand at a different location. Unless stated otherwise, we present the results using the aforementioned calibration, which allows for the observation of the gain shift and resolution degradation during irradiation. To calibrate the CZT system a flood irradiation is taken [24]. The cathode-to-anode ratio is taken to estimate the depth of interaction. Next, for a given pixel, the events are separated into multiple depth bins. The raw, uncalibrated photopeak amplitude is measured on a voxel-by-voxel basis and used to correct voxelized spectra collected in subsequent measurements.

3.2. Proton Beam Characteristics

We used the cyclotron at the Crocker Nuclear Laboratory on the University of California Davis’ campus [25]. The cyclotron can produce monoenergetic protons at various energies. This experiment utilizes a 67.5 MeV beam that passes through a Kapton window, tantalum, and aluminum diffuser. The circular beam measures 6 cm in diameter, enough to uniformly irradiate the entire M400 module. The uniformity of the beam is reported in [25] and varies less than 4% in the inner 2 cm radius.

3.2.1. Simulation of Proton Response in CdZnTe

Using a SRIM simulation [26] that accounts for the attenuation of intervening air and M400 housing we estimate a mean proton energy of 61.0 MeV impinging on the crystal. Fig. 1a shows the average energy loss of incident protons, or the electronic energy loss [26], as a function of the depth in the CdZnTe crystal using SRIM. The estimated proton range is 9.5 mm with a straggling of 227 μ m. Fig. 1b shows the two-dimensional ionization distribution of the simulated proton pencil beam.

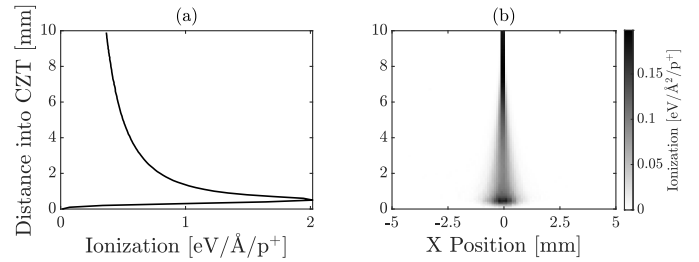


Figure 1: Simulated ionization along the path of the proton. (a) Shows the ionization projected onto the depth of the detector while (b) shows a 2D distribution of ionization. Zero depth in this plot reflects the anode.

3.3. Experimental Setup and Irradiation Plan

Two M400 modules were irradiated; one was biased and unbiased respectively during irradiation. The biased module operated at 2000 V and was acquiring spectra the entire time. The unbiased module was powered-off which disabled everything including the front-end electronics and embedded computer.

Each detector was iteratively irradiated to the prescribed fluence followed by measurement of a Cs137 check source. The source was kept in the target room throughout the experiment and placed on the cathode side - slightly off axis. The unbiased detector was turned on following irradiations to collect ¹³⁷Cs spectra and then powered off. Fig. 2 shows the experimental setup with the detector. ¹³⁷Cs spectra were collected with accumulated fluences of up to 2.6×10^8 p/cm². Using thin target approximation, this proton fluence is equivalent to ~ 45 rad(Si), or ~ 3 years on the International Space Station for an external pallet on the Columbus module: that location expects 149 mGy/yr (14.9 rad/yr) [27]. Note that the thin target approximation is not applicable in this situation, but is given a means of comparison.

Fig. 3 presents the accumulated proton dose as a function of time. The unbiased detector received its first irradiation the night before the rest of the experiment. Its date is therefore shifted such that the time elapsed is zeroed to time from the 2nd irradiation. That detector then received dosages in near-constant intervals. The biased detector also received consistent dosages except for the last two runs, which had a 2-hour gap.

4. Proton Irradiation Results

Fig. 4 plots the measured ¹³⁷Cs spectra after a given accumulated irradiation for (a) biased and (b) unbiased detectors.

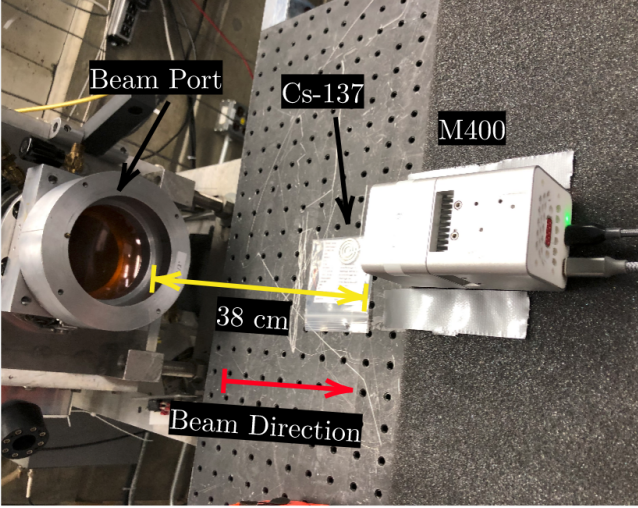


Figure 2: Experimental setup at the irradiation facility. Detectors were placed on top foam to distance them from high-Z objects.

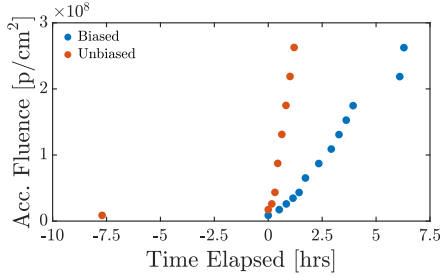


Figure 3: Irradiation history for the biased and unbiased detectors. The time elapsed signifies the time passed since the first irradiation for the biased detector. The unbiased detector is elapsed time since the second irradiation. This is due to the first irradiation in the unbiased detector taking place the night before the main experiment.

The spectra present all the events recorded by the four crystals with no event cuts applied. This includes multi-interaction events. At first glance, the peak centroid decreases, and width increases with accumulated fluence. Moreover, qualitatively, the responses appear significantly different between the biased and unbiased cases. Next, in the most degraded spectrum, we observe a ‘flat topping’ of the peak, which indicates a non-uniform response across depth. Fig. 5a plots the full width at half maximum (FWHM) as a function of the accumulated fluence. After the full prescribed irradiation of 2.6×10^8 p/cm², we observe over a factor of two poorer resolution in the biased case versus the unbiased case. The 0 accumulated fluence point is slightly off trend as it was measured at a different time and place than the rest of the data.

We observe similar behavior in Fig. 5b, which plots the peak centroid as a function of the accumulated fluence. There, after 1.7×10^8 p/cm², the centroid drifted 2.6% in the biased detector compared to 0.8% observed in the unbiased case. Note that the last two data points in the biased detector are slightly off-trend due to the 2-hour break between those sets (see Fig. 3).

The bivariate plots between energy and depth from the cathode best show the difference between the two detector’s dam-

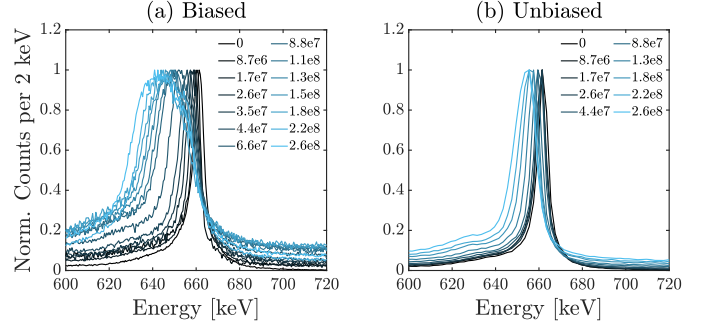


Figure 4: ¹³⁷Cs Spectra and its degradation at different accumulated fluences. (a) Presents the spectra for the biased detector while (b) presents the unbiased response.

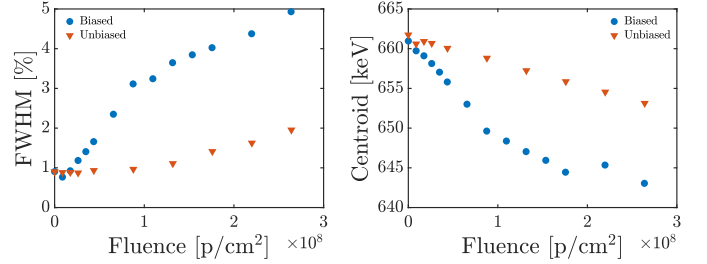


Figure 5: Quantitative features of the ¹³⁷Cs peak measurements following different fluences for the biased and unbiased detector. (a) Presents the FWHM while (b) presents the peak centroid.

age responses. Fig. 6 plots the summed ¹³⁷Cs energy-depth response for all four crystals in a given bias state. The plots treat multi-interaction events as singles. In the plots, 0 mm and 10 mm represent the cathode and anode side respectively. The most intense vertical line is the gain-shifted 662 keV line, while other lines represent internal activation. Following the 662 keV peak along the depth, we see anode side interactions have a higher gain than cathode side events. This is due to the proton-induced traps introduced along the depth of the crystal. Moreover, the response is roughly flat along the cathode side until ~ 5 mm away from the anode. This follows the dE/dx the proton experiences as shown in Fig. 1a where the ionization is roughly flat in the first ~ 5 mm from the cathode. Next, we observe a significant difference in the slope of the photopeak centroid with depth between the (a) biased and (b) unbiased cases, especially on the anode side.

5. Recovery and Annealing Studies

This section presents the recovery of the CZT detectors from annealing at room temperature and baking in a 60 °C oven. Unless stated otherwise, the displayed data uses a calibration taken pre-irradiation to display the recovery of the system relative to its original state.

5.1. Annealing

Following irradiation, the CZT detectors were stored in an office environment. In roughly a two-week cadence, we took a ¹³⁷Cs measurement to study the recovery of the detectors.

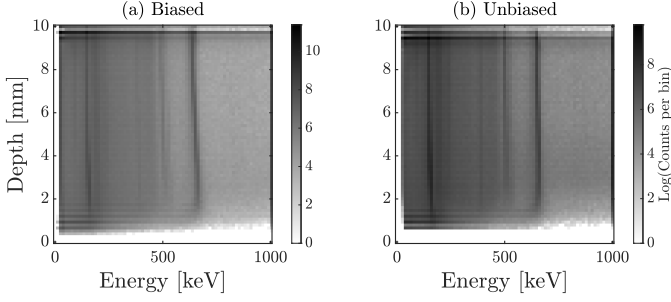


Figure 6: Depth-energy responses of a ^{137}Cs measurement following 2.6×10^8 p/cm² accumulated fluence for the (a) biased and (b) unbiased detectors. Zero depth represents the anode. Note the curvature of the ^{137}Cs peak towards the anode as cathode side events must drift through more of the defective material and are susceptible to trappings.

Fig. 7 plots the spectra for the (a) biased and (b) unbiased detectors. Fig. 8 plots the (a) peak centroid as a function of time while (b) plots the FWHM recovery. The plot shows that the first two weeks of annealing at room temperature resulted in the most significant change and reached a plateau at around 75 days. The resolution of the unbiased system plateaued to its pre-irradiated state of $\sim 1\%$, while the biased system held steady at $\sim 1.7\%$. Room temperature annealing in CZT has been previously observed in [28].

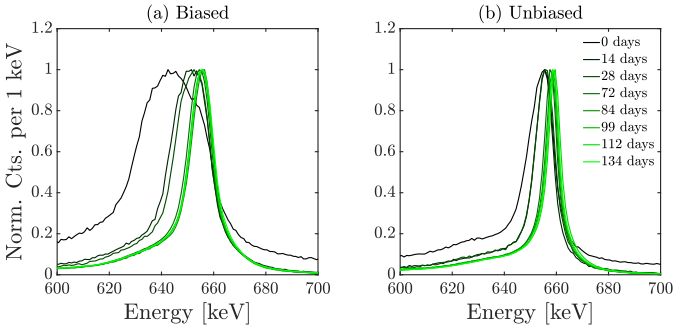


Figure 7: ^{137}Cs spectra showing recovery over time for the (a) biased and (b) unbiased case.

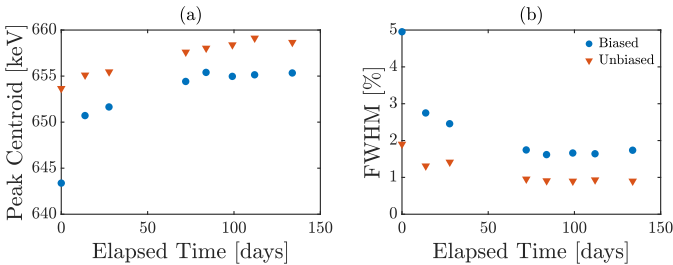


Figure 8: Recovery characteristics for the detectors annealing in room temperature. (a) plots the peak centroid over time while (b) plots the FWHM over time.

After 135 days both detectors were annealed in a 60°C three times. The sessions lasted 6, 24, and 48 hours. We chose the temperature due to several temperature limits not associated with the crystals. The detectors were then allowed to return to room temperature after which a ^{137}Cs measurement was taken.

Table 1: Summary of the radiation damaged CZT for the biased and unbiased detector after room temperature (RT) annealing and 60°C annealing. The data in the field is presented as [centroid (keV), FWHM resolution (%)].

Condition	Unbiased	Biased
0 day RT anneal	[653.7, 1.9%]	[643.3, 4.9%]
134 days RT anneal	[658.7, 0.9%]	[655.3, 1.7%]
6 hr 60°C anneal	[659.2, 0.9%]	[657.2, 1.4%]
24 hr 60°C anneal	[659.6, 0.9%]	[658.8, 1.1%]
48 hr 60°C anneal	[660.8, 1.0%]	[660.5, 0.9%]

Figure 9 plots the performance of the system after each annealing step. It shows that 78 hours in the oven was sufficient to recover the biased system to its pre-irradiated resolution. The unbiased system did not show any significant change as its resolution already recovered. Table 1 summarizes this recovery.

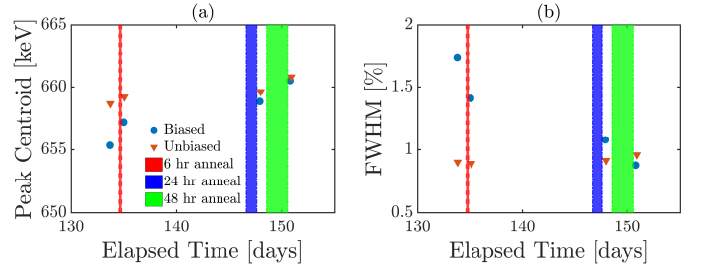


Figure 9: Recovery of the CZT detectors over several annealing sessions. The shaded time frames indicate periods in which the detectors were in the oven. (a) Plots the recovery of the peak centroid while (b) plots the FWHM.

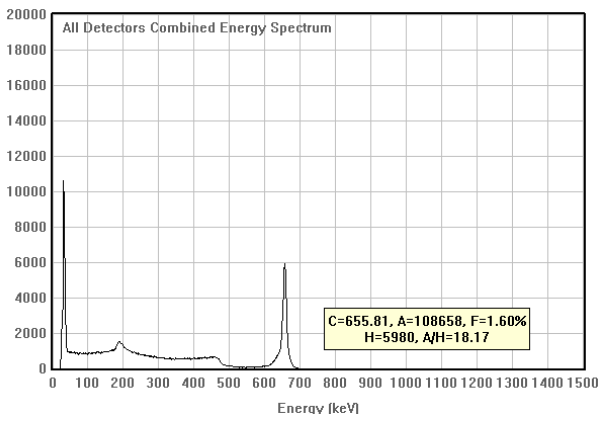
5.2. Application of Calibration

On day 50 of the room temperature recovery period, the system underwent a full calibration by H3D, Inc. With the new calibration, the biased detector's resolution improved from 1.6% to 1.23% FWHM at 662 keV, shown in Fig. 10, while Fig. 11 shows the unbiased detector's improvement from 1.4% to 1.12%. The dramatic improvement is largely due to the detector's 3D position-sensitive capabilities which allow for a voxel-by-voxel energy correction.

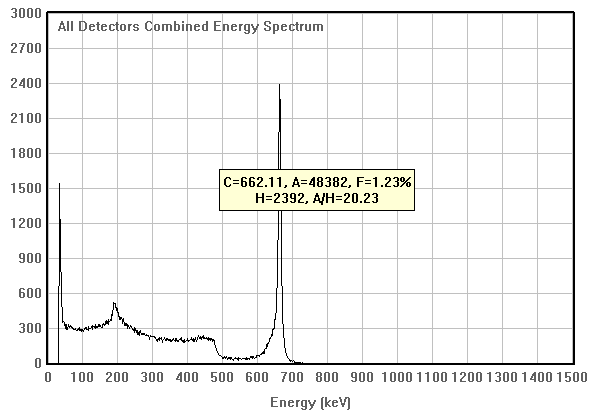
6. Activation Analysis

Immediately following the final irradiation, the CZT detectors were placed on the front face of a high-purity germanium (HPGe) detector to measure its activation products over two days. Fig. 12 shows the experimental setup. Fig. 13 shows the recorded spectra for the first 500 minutes (black solid line) and the last 500 minutes which was 2000 minutes into the measurements (dashed red line). The green dashed line represents a background measurement. The last 500 minutes show a significant reduction in internal activation with only a minor number of longer-lived products.

Table 2 lists the identified peak with the aid of InterSpec [29], with similar observation by [30, 21, 31]. The appendix of this manuscript contains additional HPGe and CZT spectral plots of

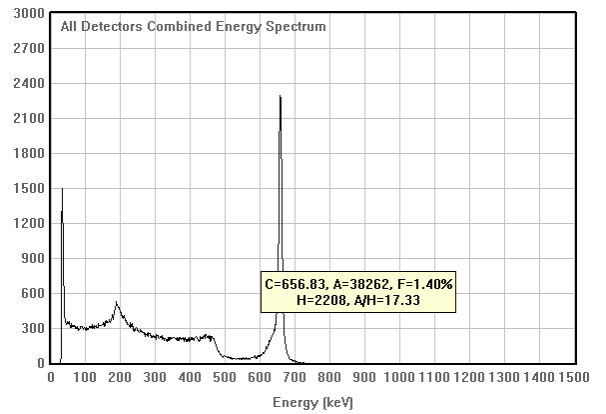


(a) Pre-calibration

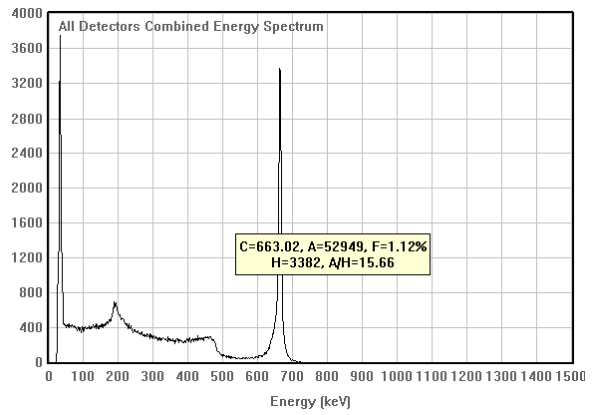


(b) Post-calibration

Figure 10: The biased detector Cs-137 spectrum (a) pre- and (b) post-calibration.



(a) Pre-calibration



(b) Post-calibration

Figure 11: The unbiased detector Cs-137 spectrum (a) pre- and (b) post-calibration.



Figure 12: Activation study setup with the CZT detector centered on the front face of the co-axial HPGe detector.

the activation. The table omits typical background lines, except for ^{24}Na lines, which is likely the result of the activated aluminum housing, as commonly observed in space missions [32].

7. Discussion

The shift in gain and degraded resolution observed during irradiation is likely a result of increased trapping sites due to bulk displacement damage which decreases the electron mobility lifetime product [33]. As such, less charge induction occurs in damaged detectors as the average charge drifting through the weighting potential decreases. We observe the decrease of electron collection efficiency with the decrease in the ^{137}Cs photopeak gain. Moreover, another result from Sec. 4 points to a possible bias dependence on radiation damage. This phenomenon is not new as other semiconductor-type devices observe this behavior [34, 35, 36, 37]. A possible explanation is that the bias of the detector may promote the drift of interstitial vacancies whereas the unbiased case may only have thermal effects for random motion. This result is, however, not consistent with a previous result conducted by Franks et al. as they report less observed damage in the biased case. This is also contradictory to the behavior of other electronics.

The results also suggest that during orbit, to preserve the performance of the instrument, crystals should remain unbiased in the SAA. This is common in many space-based instruments.

We note that when we measured the ^{137}Cs source in between irradiations, we placed the source on the cathode side. Since the Bragg peak occurred near the anode side, the majority of the damage occurred there. With a cathode side ^{137}Cs placement, a lot of the events will interact on the cathode side. Should the source be located elsewhere, changing the distribution of gamma interactions, the spectrum will look different. A polychromatic proton beam could be used to spread out the Bragg peak to mitigate this effect (i.e. spread out Bragg peak) [38].

The most dramatic recovery of the detector's performance occurred during the first two weeks. The performance recovery plateaued after 75 days with the unbiased detector's resolution returning to its original state while the biased did not. It took 78 hrs of $60\text{ }^\circ\text{C}$ annealing for the biased system's resolution to return to its original state. A full calibration of the system further

improved the system's performance, owing to the 3D position sensing capability of the detector. Note that the applied dosages in this study is more acute than what would be experienced in spaceflight. Since spaceflight might be more chronic, the detectors will continue annealing.

With a significant deadtime, the powered M400 was able to remain somewhat unparalyzed during irradiation with a flux of $\sim 10^5\text{ p/cm}^2/\text{s}$. Fig. 14 plots the recorded spectra during the first irradiation of the biased detector. Both the ^{137}Cs peak and a 511 keV peak are visible along with a continuum. The results from those irradiations are still under investigation.

8. Conclusion

This work explores the radiation damage incurred on pixelated $2 \times 2 \times 1\text{ cm}^3$ CZT detectors by 61 MeV protons. The results suggest that CZT proton radiation hardness might correlate with the detector bias during irradiation with the biased detector degrading than the unbiased detector. The biased detector began degrading, with an observable gain shift, with fluences as low as $8.7 \times 10^6\text{ p/cm}^2$ while the resolution and centroid of the unbiased detector did not degrade a fluence of $\sim 8.8 \times 10^7\text{ p/cm}^2$. The majority of proton induced degradation was recovered over a two week room temperature anneal. On day 50, a full system recalibration brought system resolutions down to 1.23% and 1.12% for the biased and unbiased detectors respectively. The recovery plateaued after ~ 75 days with the biased detector's ^{137}Cs peak located at $\sim 655.1\text{ keV}$ with 1.6% FWHM while the unbiased detector was $\sim 659.1\text{ keV}$ with 0.9%. Further annealing at $60\text{ }^\circ\text{C}$ for a period of 78 hours allowed for the full resolution recovery of the system to its pre-irradiated state.

We are still investigating the response of the CZT detector when it was acquiring during irradiation. Finally, we are currently developing an instrument using $4 \times 4 \times 1.5\text{ cm}^3$ pixelated CZT detectors with a slated launch date of early 2025 to the International Space Station. The project aims to space-qualify the large-volume crystals and associated electronics and study their operations in a space environment.

Acknowledgment

We appreciate the efforts of Michael Backfish and the Crocker Nuclear Laboratory staff for ensuring a successful experiment. This work is supported by the Office of Naval Research 6.1. D. Shy is supported by the U.S. Naval Research Laboratory's Jerome and Isabella Karle Fellowship.

The H3D, Inc. portions of this work were funded under the Department of Energy Small Business Innovative Research Program award number DE-SC0021765.

Appendix A. CZT Measurement of Internal Activation

The CZT system is also able to intrinsically measure internal activation. Fig. A.15 plots the response of two-interaction events for a ^{137}Cs measurement taken right after irradiation. Since CZT does not have the timing resolution to distinguish

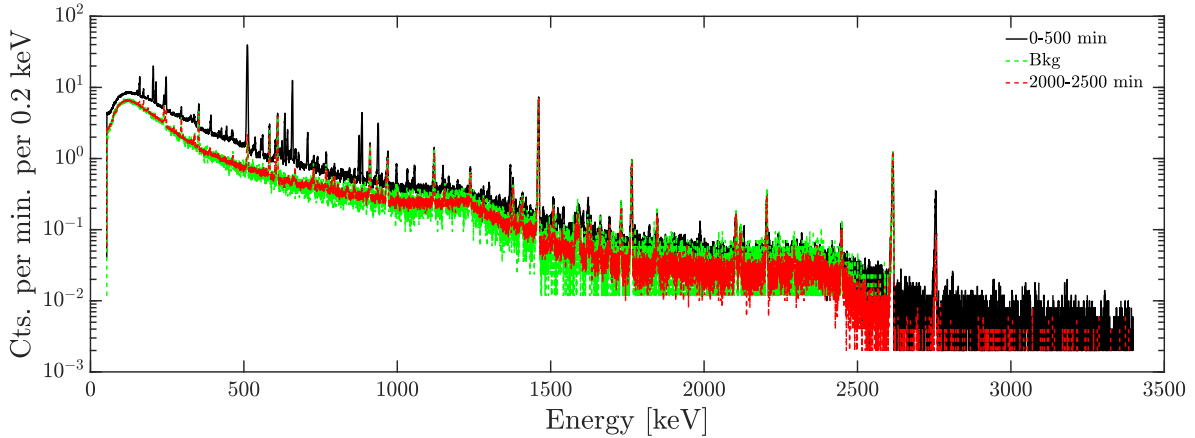


Figure 13: Full HPGe spectrum of the CZT detector taken after irradiation.

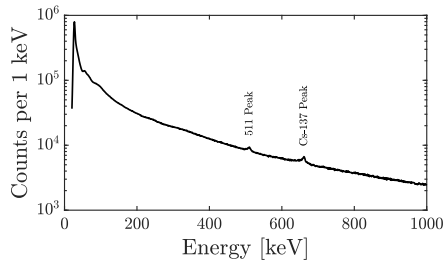


Figure 14: Spectra from when the detector was biased and acquiring during the first irradiation.

between interactions, the temporal order of interactions cannot be resolved. The labeling of interactions 1 and 2 are therefore arbitrary and interchangeable. In the plot, diagonals such as those indicated 511 and 662 keV, represent gamma rays that scatter and are subsequently absorbed in CZT. A portion of the horizontal and vertical events at 511 keV as one of the interactions may be represented by a β^+ decay. There, the continuum represents the positron's kinetic energy, which will then annihilate to produce two 511 keV photons. In this plot, one of the annihilation photons escaped. A coincident background event and a 511 keV measurement could also contribute to the distribution. The two islands of events labeled as In111 originate from measuring the 171.3 and 245.4 keV photons simultaneously.

Finally, we plot the full gamma-ray spectrum of the ^{137}Cs source over time in Fig. A.16 as taken by the CZT detectors during the recovery study. After two weeks, the spectra show the majority of internal activation has decayed.

Appendix B. Additional HPGe Plots

This appendix offers additional plots taken by the HPGe to study the activation productions. Fig. B.17 presents a waterfall plot showing the time evolution of the gamma-ray spectrum. The energy range is divided into two to highlight the different regions (top and bottom).

Figs. B.18, B.19, B.20, B.21 present the HPGe spectra with different energy ranges comparing the first 500 minutes, the

gamma-ray background, and the last 500 minutes of the measurements which were 2000 minutes into the measurement.

References

- [1] G. Knoll, Radiation Detection and Measurement, Wiley, 2010.
- [2] K. R. Slavis, et al., High-altitude balloon flight of CdZnTe detectors for high-energy x-ray astronomy: II, in: O. H. W. Siegmund, K. A. Flanagan (Eds.), EUV, X-Ray, and Gamma-Ray Instrumentation for Astronomy X, Vol. 3765, International Society for Optics and Photonics, SPIE, 1999, pp. 397 – 406. doi:10.1117/12.366520. URL <https://doi.org/10.1117/12.366520>
- [3] J. A. Jenkins, T. Narita, J. E. Grindlay, P. F. Bloser, C. M. Stahle, B. H. Parker, S. D. Barthelmy, Background measurements from balloon-born imaging CZT detectors, in: J. E. Truemper, H. D. Tananbaum (Eds.), SPIE Proceedings, SPIE, 2003. doi:10.1117/12.461537. URL <https://doi.org/10.1117/12.461537>
- [4] N. Auricchio, L. Abbene, G. Benassi, M. Bettelli, A. Buttacavoli, S. Del Sordo, F. Principato, N. Sarzi Amadè, J. Stephen, N. Zambelli, S. Zanetini, A. Zappettini, E. Caroli, A CZT 3D imaging spectrometer prototype with digital readout for high energy astronomy, Nuclear Instruments and Methods in Physics Research Section A: Accelerators, Spectrometers, Detectors and Associated Equipment 1047 (2023) 167869. doi:<https://doi.org/10.1016/j.nima.2022.167869>. URL <https://www.sciencedirect.com/science/article/pii/S0168900222011615>
- [5] S. D. Barthelmy, et al., The Burst Alert Telescope (BAT) on the SWIFT Midex Mission, Space Science Reviews 120 (3-4) (2005) 143–164. doi:10.1007/s11214-005-5096-3. URL <https://doi.org/10.1007/2Fs11214-005-5096-3>
- [6] V. Bhalerao, D. Bhattacharya, A. Vibhute, P. Pawar, A. R. Rao, M. K. Hingar, R. Khanna, A. P. K. Kuty, J. P. Malkar, M. H. Patil, Y. K. Arora, S. Sinha, P. Priya, E. Samuel, S. Sreekumar, P. Vinod, N. P. S. Mithun, S. V. Vadawale, N. Vagshette, K. H. Navalgund, K. S. Sarma, R. Pandiyan, S. Seetha, K. Subbarao, The Cadmium Zinc Telluride Imager on AstroSat, Journal of Astrophysics and Astronomy 38 (2). doi:10.1007/s12036-017-9447-8. URL <https://doi.org/10.1007/2Fs12036-017-9447-8>
- [7] T. Prettyman, W. Feldman, K. Fuller, S. Storms, S. Soldner, C. Szles, F. Ameduri, D. Lawrence, M. Browne, C. Moss, CdZnTe gamma-ray spectrometer for orbital planetary missions, IEEE Transactions on Nuclear Science 49 (4) (2002) 1881–1886. doi:10.1109/TNS.2002.801672.
- [8] N. Østgaard, et al., The Modular X- and Gamma-Ray Sensor (MXGS) of the ASIM Payload on the International Space Station, Space Science Reviews 215 (2). doi:10.1007/s11214-018-0573-7. URL <https://doi.org/10.1007/2Fs11214-018-0573-7>
- [9] J. McEnery, et al., All-sky Medium Energy Gamma-ray Observatory: Exploring the Extreme Multimessenger Universe (2019). doi:10.48550/

Table 2: Identified radioisotopes in the activation spectrum taken by the HPGe detector. Along with the isotope, we report the energy, branching ratio, and half-life. The units for the half-life have the following short hand: m-minutes, h-hours, and d-days.

Isotope	Energy [keV]	Branch Ratio [%]	Half Life	Isotope	Energy [keV]	Branch Ratio [%]	Half Life
Ag104	555.8	92.6	69.2m	In-110	461.8	4.718	4.9h
Cd-111m	150.82	29.14	48.5m		560.32	1.867	
	254.4	94.0	48.5m		581.93	8.551	
I-121	212.2	84.3	127.2m		584.21	6.487	
I-123	158.97	83.3	13.22h		641.68	25.95	
I-124	602.73	62.9	4.18d		657.75	98.29	
	722.78	10.36			677.6	4.521	
	1690.96	11.15			707.4	29.49	
I-126	666.33	32.88	12.93d		744.26	1.966	
	753.82	4.147			759.87	3.145	
I-128	442.9	12.62	24.99m		818.02	2.261	
I-130	417.93	34.15	12.36h		844.67	3.244	
	536.07	99.0			884.67	92.88	
	668.54	96.03			901.53	1.966	
	739.51	82.17			937.48	68.41	
In-107	204.95	47.2	32.4m		997.16	10.52	
In-108	1032.8	35.35	58.0m	In-110m	2129.4	2.158	69.1m
	1056.6	28.77			2211.33	1.746	
	1299.3	15.07			2317.41	1.29	
	1485.8	4.384		In-111	171.28	90.65	67.31h
	1606.3	8.494			245.35	94.08	
In-108m	632.9	76.4	39.6m	In-111m	537.0	87.2	7.7m
	875.4	2.445		In-113m	391.7	64.94	99.48m
	1529.4	7.334		In-116m	1293.4	84.8	54.29m
	1986.3	12.38			1507.59	9.922	
In-109	203.5	73.5	4.17h	Na-24	1368.63	100	14.9h
	288.4	1.617			2754.03	99.94	
	347.5	2.131		Te-121	573.14	80.4	19.17d
	426.2	4.116					
	613.6	2.278					
	619.0	1.764					
	623.5	5.513					
	649.8	1.604					
	949.1	1.313					
	1049.7	1.169					
	1149.1	4.337					
	1196.5	1.617					
	1272.9	0.5586					
1419.2	1.264						
1475.8	0.441						

ARXIV.1907.07558.

URL <https://arxiv.org/abs/1907.07558>

- [10] E. Orlando, et al., Exploring the MeV sky with a combined coded mask and Compton telescope: the Galactic Explorer with a Coded aperture mask Compton telescope (GECCO), *Journal of Cosmology and Astroparticle Physics* 2022 (07) (2022) 036. doi:10.1088/1475-7516/2022/07/036.

URL <https://dx.doi.org/10.1088/1475-7516/2022/07/036>

- [11] M. Moita, L. Ferro, E. Caroli, E. Virgilli, F. Frontera, J. B. Stephen, R. M. Curado Da Silva, J. M. Maia, S. Del Sordo, ASTENA's Polarimetric Prospects, in: 2021 IEEE Nuclear Science Symposium and Medical Imaging Conference (NSS/MIC), 2021, pp. 1-7. doi:10.1109/NSS/MIC44867.2021.9875607.

- [12] L. Kurnosova, T. Kolobyanina, V. Logachev, L. Razorenov, I. Sirotkin, M. Fradkin, Discovery of radiation anomalies above the South Atlantic at heights of 310-340 km, *Planetary and Space Science* 9 (8) (1962) 513-516. doi:[https://doi.org/10.1016/0032-0633\(62\)90057-0](https://doi.org/10.1016/0032-0633(62)90057-0). URL <https://www.sciencedirect.com/science/article/pii/0032063362900570>

- [13] E. Stassinopoulos, J. Raymond, The space radiation environment for electronics, *Proceedings of the IEEE* 76 (11) (1988) 1423-1442. doi:10.1109/5.90113.

- [14] F. Lebrun, J.-P. Roques, A. Sauvageon, R. Terrier, P. Laurent, O. Limousin, F. Lugiez, A. Claret, INTEGRAL: In flight behavior of ISGRI and SPI, *Nuclear Instruments and Methods in Physics Research Section A: Accelerators, Spectrometers, Detectors and Associated Equip-*

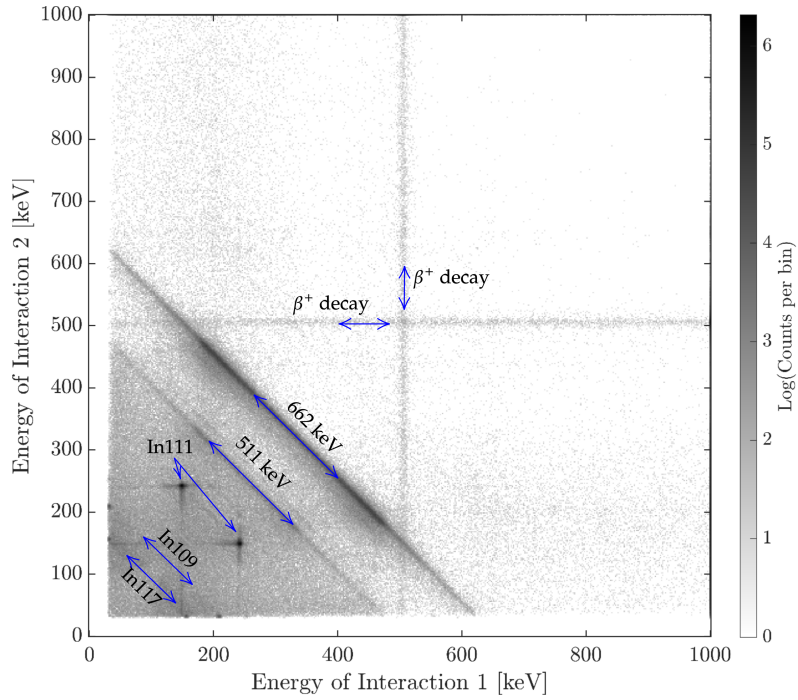


Figure A.15: Bivariate plot of two-interaction events of a ^{137}Cs measurement taken right after the full proton irradiation with the 'biased' detector.

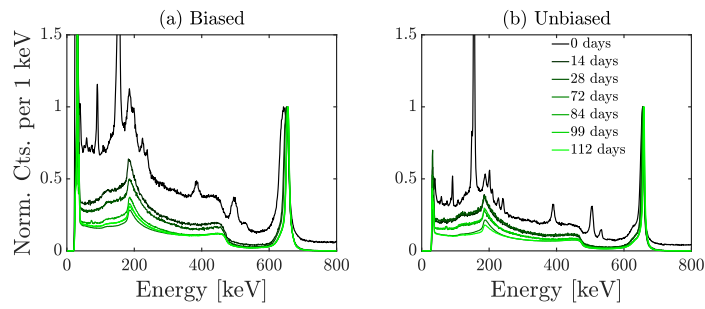


Figure A.16: Change of spectrum over time following irradiation. Note that the ^{137}Cs source location and environmental factors were not controlled between different measurements. This plot is the same as Fig. 7, just with a larger energy range to display the internal activation.

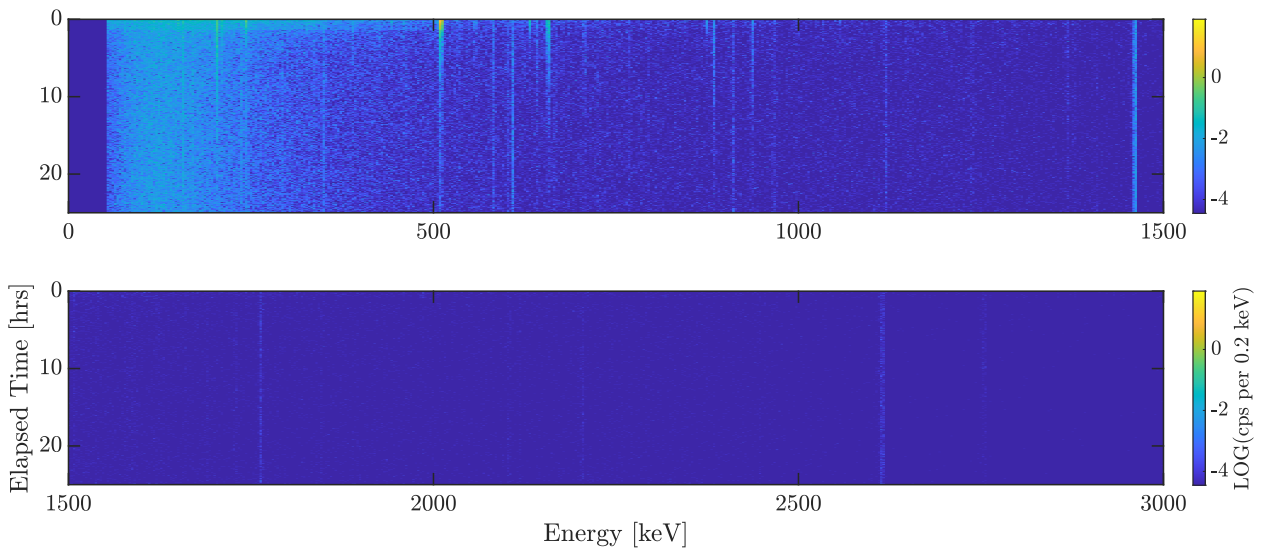


Figure B.17: Spectrogram of the gamma-ray spectrum over time

10.1016/0969-806X(94)90203-8.

URL <https://www.sciencedirect.com/science/article/pii/S0969806X94902038>

- [35] M. K. Tiwari, J. Diwan, S. K. Singh, A. Topkar, Comparison of Gamma Radiation Effects on CCD Cameras under Different Bias Conditions using Image Analysis Techniques, *IEEE Transactions on Nuclear Science* (2022) 1–doi:10.1109/TNS.2022.3222714.
- [36] V. Cindro, G. Kramberger, M. Mikuž, M. Tadel, D. Žontar, Bias-dependent radiation damage in high-resistivity silicon diodes irradiated with heavy charged particles, *Nuclear Instruments and Methods in Physics Research Section A: Accelerators, Spectrometers, Detectors and Associated Equipment* 450 (2) (2000) 288–296. doi:[https://doi.org/10.1016/S0168-9002\(00\)00258-8](https://doi.org/10.1016/S0168-9002(00)00258-8).
URL <https://www.sciencedirect.com/science/article/pii/S0168900200002588>
- [37] R. M. Zedric, S. S. Chirayath, C. M. Marianno, Y. Diawara, N. Skukan, Bias-dependent displacement damage effects in a silicon avalanche photodiode, *Nuclear Instruments and Methods in Physics Research Section B: Beam Interactions with Materials and Atoms* 507 (2021) 42–45. doi:<https://doi.org/10.1016/j.nimb.2021.09.013>.
URL <https://www.sciencedirect.com/science/article/pii/S0168583X21003001>
- [38] M. P. Páscoa, J. M. Maia, N. Auricchio, R. M. Curado da Silva, P. Crespo, S. J. C. do Carmo, M. Moita, F. Alves, E. Caroli, Orbit-Like Proton Radiation Sensitivity of CdTe Detectors: Evaluation of Mobility-Lifetime Products and Spectroscopic Properties, *IEEE Transactions on Nuclear Science* 66 (9) (2019) 2063–2071. doi:10.1109/TNS.2019.2935119.
- [39] A. Wong, F. A. Harrison, L. S. Varnell, Effects of proton-induced radiation damage on cadmium zinc telluride pixel detectors, in: B. D. Ramsey, T. A. Parnell (Eds.), *Gamma-Ray and Cosmic-Ray Detectors, Techniques, and Missions*, Vol. 2806, International Society for Optics and Photonics, SPIE, 1996, pp. 442 – 448. doi:10.1117/12.254016.
URL <https://doi.org/10.1117/12.254016>